Polarity-driven oxygen vacancy formation in ultrathin $LaNiO_3$ films on $SrTiO_3$

I-Cheng Tung,[1,2] Guangfu Luo,[3] June Hyuk Lee,[4] Seo Hyoung Chang,[5] Jarrett Moyer,[6] Hawoong Hong,[1] Michael J. Bedzyk,[2,7] Hua Zhou,[1] Dane Morgan,[3] Dillon D. Fong,[5] and John W. Freeland[1,*]

[1]*Advanced Photon Source, Argonne National Laboratory, Argonne, Illinois 60439, USA*

[2]*Department of Materials Science and Engineering, Northwestern University, Evanston, Illinois 60208, USA*

[3]*Department of Materials Science and Engineering, University of Wisconsin, Madison, Wisconsin 53706, USA*

[4]*Neutron Science Division, Korea Atomic Energy Research Institute, Daejeon 305-600, Republic of Korea*

[5]*Materials Science Division, Argonne National Laboratory, Argonne, Illinois 60439, USA*

[6]*Department of Physics and Materials Research Laboratory, University of Illinois, Urbana-Champaign, Illinois 61801, USA*

[7]*Department of Physics and Astronomy, Northwestern University, Evanston, Illinois 60208, USA*

(Received 30 November 2016; revised manuscript received 3 April 2017; published 18 October 2017)

Oxide heterostructures offer a pathway to control emergent phases in complex oxides, but their creation often leads to boundaries that have a polar discontinuity. In order to fabricate atomic-scale arrangements of dissimilar materials, we need a clear understanding of the pathways by which materials resolve polarity issues. By examining the real-time lattice structure *in situ* during growth for the case of polar $LaNiO_3$ synthesized on nonpolar $SrTiO_3$ (001), we demonstrate how films in ultrathin limit form as $LaNiO_{2.5}$ and then evolve into $LaNiO_3$ as the thickness increases. Theory explains how the polar energetics drives the formation of oxygen vacancies and the stability of these phases with thickness and structure.

DOI: 10.1103/PhysRevMaterials.1.053404

I. INTRODUCTION

Correlated transition-metal oxides host a diverse array of electronic and magnetic properties, including high-temperature superconductivity, colossal magnetoresistance, ferroelectricity, and Mott metal-insulator transitions (MITs) [1]. The atomic-level synthesis of functional oxides and an understanding of their growth behavior provide opportunities to explore and control the intriguing properties of artificial oxide heterostructures [2–4]. The main challenge, however, is to understand how to create the desired material structure at the unit-cell (u.c.) level in coordination with highly dissimilar materials or unfavorable surface terminations. One of the specific problems in oxide heterostructures is how to manage high-energy charge configurations at surfaces and interfaces, which is most difficult for the case of polar materials and surfaces (i.e., charge arrangements that lead to a nonzero electric field between the layers). From a classical charge standpoint, the main problem stems from the noncompensated electric fields created externally or across an interface, known as the polar discontinuity. This is a well-known problem for the case of surfaces [5,6] and semiconductor interfaces [7] and has been explored extensively in the past decade in the context of oxide interfaces [8–12]. However, it is clear that in the case of oxides, several material-specific routes exist to resolve the energy at the surface that depend on not only the chemical coordination but also on the ability of ions to change valence state as well as the energy for the formation of defects [13,14].

For the case of trivalent nickelate heterostructures (e.g., $LaNiO_3$), this is particularly important given the predictions of emergent phases such as superconductivity, which can arise in strongly confined ultrathin heterostructures [15–17]. However, the realization of these structures requires the fabrication of ultrathin nickelate layers and understanding how the properties evolve with thickness. For the case of $LaNiO_3$ prepared on polar substrates [e.g., $LaAlO_3$ (LAO)], it is clear that metallic phases can be realized even down to few u.c. thickness [18–20], in confined geometries [21,22], or under tensile strain with polar buffer layers [23]. On the other hand, $LaNiO_3$ prepared directly on nonpolar $SrTiO_3$ (STO) (001) shows a metal-insulator transition at larger thicknesses indicating that something fundamentally different is occurring for the case with a polar mismatch at the interface [24–27], which some work had connected with the formation of nonstoichiometric $LaNiO_3$ in ultrathin layers [28–31].

In this paper, we have explored the effect of the polar discontinuity on the structure and properties of epitaxial $LaNiO_3$ ultrathin films on STO (001) by using *in situ* surface x-ray diffraction during oxide molecular beam epitaxy and *ex situ* x-ray absorption spectroscopy. Structural studies for a series of final thicknesses (4–11 u.c.) show a clear evolution in the lattice structure that is connected with the formation of Ni^{2+}, likely due to the creation of oxygen vacancies in the ultrathin films (4–6 u.c.), which then fill in to form the stoichiometric Ni^{3+} state when the layer thickness increases. Theoretical calculations based on density functional theory (DFT) predict the stable structure of the defective phase and find good agreement with the experimental observations. These trends demonstrate that surface polarity can dramatically change defect concentration in thin films, yielding different valence, conductivity, and phase, as well as associated changes in structure, as a function of film thickness.

II. EXPERIMENTS

The *in situ* growth experiments were performed using reactive oxide molecular beam epitaxy [32] in an oxide chamber at beamline 33-ID-E of Advanced Photon Source (APS) [33]. Here, we synthesized atomically defined layers of the $LaNiO_3$ down to single pseudocubic u.c. thickness, epitaxially stabilized on STO (001) substrates. The $LaNiO_3$

*freeland@anl.gov

films were grown at 590 °C and in a background pressure of 8×10^{-6} Torr in a mixture of 10% ozone and 90% oxygen using La and Ni effusion cells. Both sources were shuttered to deposit alternating monolayer doses of LaO and NiO_2. Shutter times were initially set based on flux measurements made using a quartz crystal microbalance, and then checked by optimizing Kiessig (thickness) fringes with a high-resolution x-ray reflection measurement on a calibration sample immediately prior to the growth of the sample sets. Before growth, STO substrates were prepared using a termination recipe to achieve a TiO_2-terminated surface [34]. The *in situ* surface x-ray diffraction measurements were performed using a monochromatic 15 keV x-ray beam and measured under the growth conditions. Soft x-ray absorption spectra were taken at room temperature at beamline 4-ID-C of APS. Transport measurements were performed in the van der Pauw configuration upon cooling from 350 to 2 K. Each sample was patterned with gold electrodes and then indium bonded to gold wires in a way suitable for four-point resistance measurements.

III. RESULTS AND DISCUSSIONS

A series of epitaxial ultrathin $LaNiO_3$ films of different thickness (ranging from 4 to 11 u.c.) were grown on STO (001) substrates, and high-resolution x-ray scattering was recorded along the out-of-plane direction (00L) crystal truncation rod (CTR) under growth conditions immediately following the deposition. The x-ray results are shown in Fig. 1(a), where the substrate Bragg peaks have been omitted for the explicitness of CTR. Post-growth measurements confirm that the films are all coherently strained. To gain further insight into the structural quality and the chemical phase obtained during the initial growth sequence, CTR was also taken on the 11 u.c. film immediately after approximately 5 u.c. of growth under growth conditions. We also measured the effect of the polar mismatch at the heterointerface on the electrical resistivity of ultrathin $LaNiO_3$ films. As shown in Fig. 1(b), the resistivity versus temperature behavior shows bulklike metallic behavior down to low temperature for the 11 u.c. film. The magnitude and shape are consistent with other reports on ultrathin films of $LaNiO_3$ [35–37]. However, as the film thickness decreases, the resistivity increases. The 6 u.c. film exhibits insulating (semiconducting) behavior starting from room temperature, and 4 u.c. film becomes highly insulating with the resistivity that is two orders of magnitude higher than 6 u.c. film, which demonstrates the development of a new electronic ground state of the material. Previous work showed a crossover between metal and insulator at ∼5 u.c. and was linked to the effect of a dimensional crossover from three to two dimensions [24]. Below we will show the origin of this MIT results from a polarity-driven change in the oxygen stoichiometry.

To better understand the thickness-dependent MIT, we tracked the evolution in electronic structure using x-ray absorption spectroscopy (XAS). As shown in Fig. 1(c), resonant x-ray absorption was performed at the Ni L_2 edge in the bulk-sensitive fluorescence yield mode to determine changes in the electronic structure and charge state of Ni as a function of the $LaNiO_3$ thickness. A comparison of the line shape and

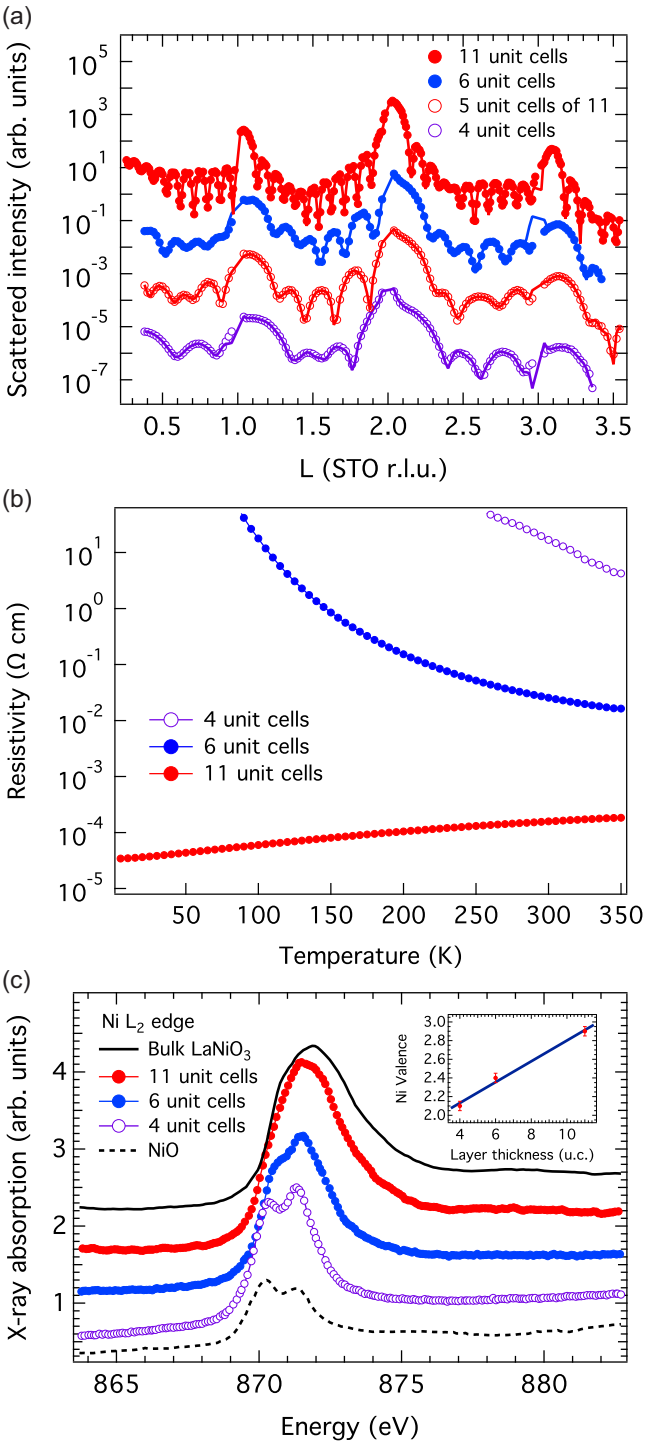

FIG. 1. (a) X-ray scattering from a series of $LaNiO_3$ films with varying thickness measured immediately following the growth of the final layer under growth conditions and for the 11 u.c. (final) film structure measured immediately following the growth of fifth u.c. Solid lines are a fit to the data discussed in the text. (b) Temperature dependence from 2 to 350 K of film resistivity showing that the 11 u.c. film is metallic as expected but 6 and 4 u.c. films are insulating. (c) X-ray absorption at the Ni L_2 edge was used to determine the sample valence. The inset shows the Ni valence varied from Ni^{2+} when the films are very thin to the expected bulk Ni^{3+} value by 11 u.c.

the L_2 energy position (i.e., the chemical shift) for the $LaNiO_3$ films with a Ni^{2+} material, NiO, and a Ni^{3+} bulk $LaNiO_3$ sample [38] indicates that Ni ions are indeed close to the 2+ oxidation state for thinner films, and the relative weight of Ni^{3+} ions increases progressively with the film thickness. The changes in Ni valence are presumably due to changes in oxygen vacancy concentration, as oxygen vacancies are the most active defect that can drive Ni redox. As seen in the inset of Fig. 1(c), the oxidation state changes linearly with thickness. The 2+ valence in the 4 u.c. film is consistent with the formation of $LaNiO_{2.5}$ during the initial growth, which then gradually absorbs oxygen to form a stoichiometric film with increasing thickness. Since we measured the valence of the entire film in all cases, we can estimate the average stoichiometry and fraction of Ni^{2+} and Ni^{3+} in the film. For a film of 11 u.c., there cannot be more than 1–2 u.c. Ni^{2+} or the valence would not be close to Ni^{3+}. As we will show below, this means that the initial layer of 4 u.c. of $LaNiO_{2.5}$ has been converted during the growth to a stoichiometric phase as the film thickness increases to beyond 11 u.c.

To gain insight into the lattice structure and its evolution with thickness, the CTRs were all quantified using the one-dimensional coherent Bragg rod analysis (COBRA) technique [39]. The resulting electron densities for these films after growth of the final layer are shown in Fig. 2(a). This plot shows the results for these films after growth of the final layer. The pseudocubic c-axis lattice parameter, c_L, and the B-site displacement, ΔB, extracted from fitting the peak positions of the electron densities are shown in Figs. 2(b) and 2(c), respectively. It is important to note that the average lattice constant determined by measuring the position of the (003) peak for the films of 6 u.c. and thinner would lead us to believe that the average lattice parameter is much smaller than it actually is as seen by the average of the layer resolved results. This apparent discrepancy is due to a strong interaction between the Kiessig fringes and the gradient of c_L. As a reference, the $R3c$ form of $LaNiO_3$ has a pseudocubic lattice parameter of 3.83 Å, which means films on STO are under $\sim 2\%$ tensile strain. The literature has shown an expected c-axis value of $\sim$ 3.80 Å [36,40–42] and $LaNiO_{2.5}$ on STO has an average c-axis parameter of $\sim$3.73 Å [43,44]. Furthermore, there is a strong polar displacement of the BO_2 layer (ΔB) away from the unit-cell center. The gradient of lattice parameter and polar distortions are similar to those seen in the case of LAO on STO [45–50], which was also attributed to polar-mismatch-driven distortions. The ΔB will be discussed more below in connection to interfacial charge transfer.

Additionally, included in Fig. 2 are data taken on the 11 u.c. film after approximately 5 u.c. of growth. The purpose of this data was to understand not only how the films evolved as a function of final thickness, but during the growth as well. Following the trend of the lattice parameter and B-site displacement shown in Figs. 2(b) and 2(c), it is clear that a similar lattice structure that occurred in the 4 u.c. film was present in the 11 u.c. sample at the early stages of growth. This comparison allows us to see that the films start oxygen deficient, but as they grow in thickness, they convert into the proper $LaNiO_3$ phase. As noted in the discussion of the XAS, even though the film was $LaNiO_{2.5}$ at 4 u.c., by the time the film is 11 u.c., it has almost fully converted to the desired $LaNiO_3$ phase.

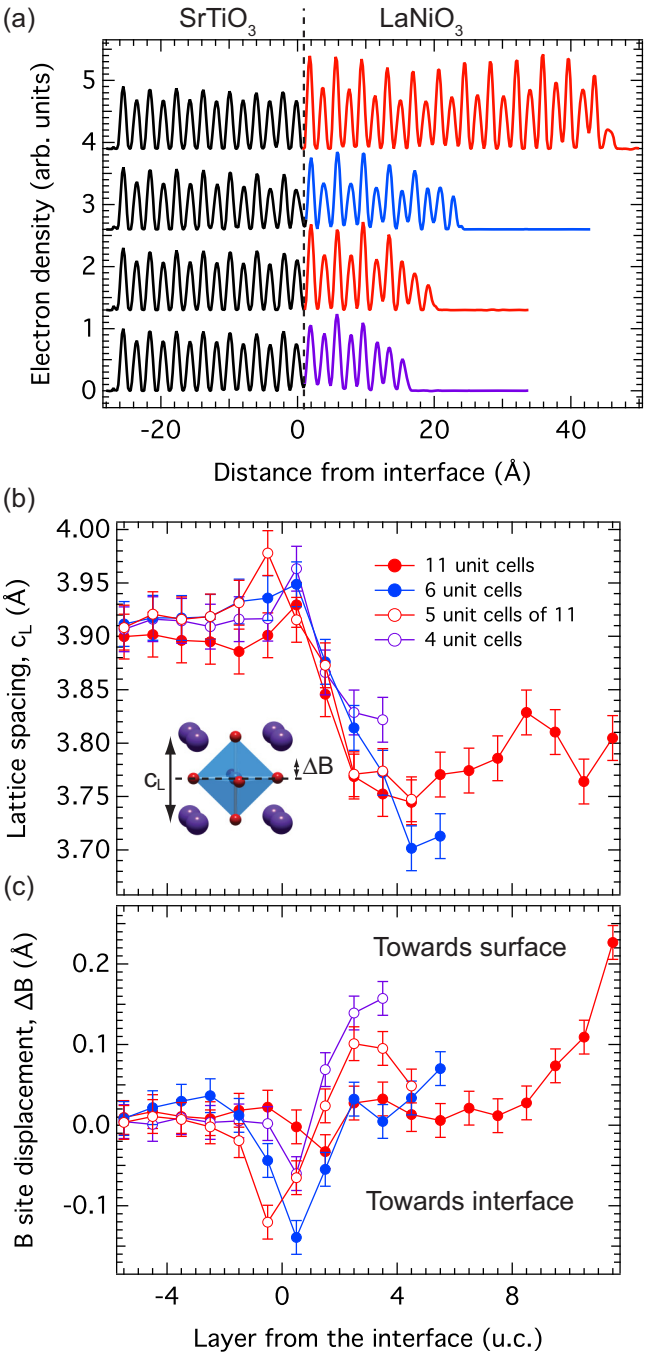

FIG. 2. (a) Electron density profiles determined by COBRA analysis of the data for the 11 u.c. film (red), 6 u.c. film (blue), and 4 u.c. film (violet). The electron density profile for the 11 u.c. (final) film structure measured after 5 u.c. of growth is also shown in red. Layer-dependent evolution of (b) pseudocubic lattice parameter, c_L, and (c) the B-site displacement, ΔB, across the interface. The inset shows a pseudocubic unit cell denoting the two parameters shown in the plots.

To understand the oxygen loss in the ultrathin limit, *ab initio* calculations were performed using DFT, as coded in the Vienna *ab initio* Simulation Package (VASP) [51,52]. The Perdew-Burke-Ernzerhof functional was employed and the projector augmented wave method was utilized with the following

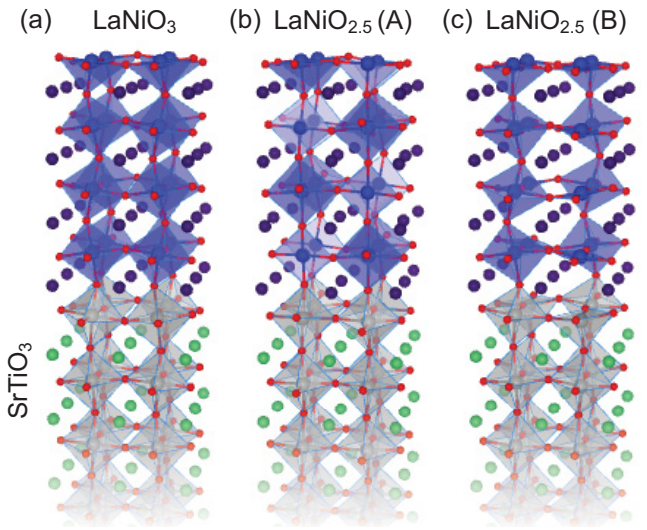

FIG. 3. 4-u.c. epitaxial (a) $LaNiO_3$, (b) $LaNiO_{2.5}$ (A) and (c) $LaNiO_{2.5}$ (B) on STO substrate. V_O resides in the NiO_2 or LaO layers that are parallel or perpendicular to the interface for $LaNiO_{2.5}$ (A) and $LaNiO_{2.5}$ (B), respectively.

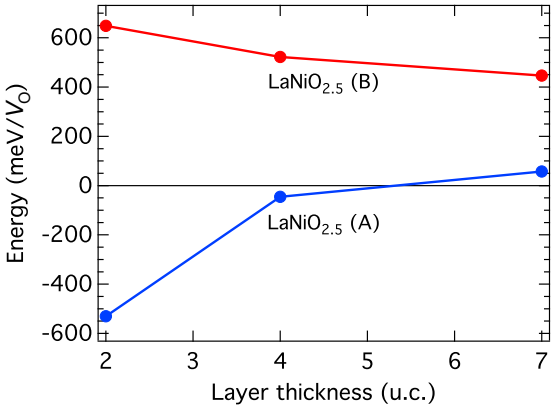

FIG. 4. Formation energy of epitaxial $LaNiO_{2.5}$ with respect to epitaxial $LaNiO_3$ under the experimental temperature and oxygen environment.

potentials: O ($2s^2 2p^4$, $E_{cut} = 400.0$ eV), Ti ($3s^2 3p^6 3d^2 4s^2$, $E_{cut} = 274.6$ eV), Ni ($3p^6 3d^8 4s^2$, $E_{cut} = 367.9$ eV), Sr ($4s^2 4p^6 5s^2$, $E_{cut} = 229.3$ eV), and La ($5s^2 5p^6 5d^1 6s^2$, $E_{cut} = 219.3$ eV). To describe the localized d electrons in Ni, an effective Hubbard U value of 6.4 eV was applied per previous studies [53,54]. The plane-wave energy cutoff was set to 500 eV. To simulate the epitaxial films, the substrate was approximated with a 2.4-nm-thick slab of cubic $SrTiO_3$, with the bottom four atomic layers fixed to the bulk positions and the other layers relaxed. A 1.5-nm-thick vacuum slab was added to reduce the mirror interactions between neighboring supercells. The supercell in the plane consists of 2×2 times of the cubic primitive cell and a $3 \times 3 \times 1$ Monkhorst-Pack k-point grid was adopted accordingly. A detailed discussion on the correction to the overbinding error and the chemical potential used in our calculations is described in the Supplemental Material [55].

The starting point for the modeling was to consider potential crystal structures that would form based upon knowledge of bulk $LaNiO_3$ and $LaNiO_{2.5}$ [56,57]. Figure 3 shows the structure of $LaNiO_3$ [Fig. 3(a)] and that of $LaNiO_{2.5}$, which has two different possible unit-cell orientations relative to the $SrTiO_3$ substrate that are labeled as (A) and (B), as shown in Figs. 3(b) and 3(c), respectively. While $LaNiO_3$ contains one Ni site with octahedral coordination of oxygen, the $LaNiO_{2.5}$ phase consists of alternating octahedral and planar coordinated Ni sites, where $LaNiO_{2.5}$ (A) and $LaNiO_{2.5}$ (B) correspond to orienting the planar Ni sites parallel and perpendicular to the growth axis (surface normal), respectively. Orienting the spatial alignment of different coordination sites to lower the strain has been observed in other systems (e.g., cobaltites [58,59]).

To understand oxygen vacancy (V_O) formation in the epitaxial films, we theoretically examined the stability of $LaNiO_{2.5}$ relative to $LaNiO_3$ at the oxygen chemical potential used in the experiments, as detailed in the Supplemental Material [55]. Figure 4 shows that in the examined thickness range, the formation energy of $LaNiO_{2.5}$ (B) is always positive, indicating that $LaNiO_{2.5}$ (B) is less stable than $LaNiO_3$. By contrast, $LaNiO_{2.5}$ (A) has negative formation energies for the structures with 2 and 4 u.c., suggesting that the $LaNiO_{2.5}$ (A) is more stable than the corresponding $LaNiO_3$ for these two thicknesses. The formation of $LaNiO_{2.5}$ (A) becomes more difficult relative to $LaNiO_3$ with increasing thickness and a complete transition to $LaNiO_3$ is predicted to occur at a thickness of 6 u.c. This prediction of structural transition is qualitatively consistent with the experimental observation of charge state evolution from Ni^{2+} to Ni^{3+} with increasing thickness [Fig. 1(c)]. However, there is some quantitative discrepancy, as the transition to complete $LaNiO_3$ occurs experimentally at 11 u.c. rather than 6 u.c. This discrepancy is not surprising given the uncertainty in the oxygen chemical potential (see Supplemental Material [55]) and the fact that the experimental transition to $LaNiO_3$ involved a relatively smooth increase in oxygen content of the film [Fig. 1(c)], while our model treated only ideal cases of perfect $LaNiO_{2.5}$ and $LaNiO_3$. Since bulk $LaNiO_{2.5}$ is highly insulating (2.0 eV band gap from our calculations) while $LaNiO_3$ is metallic (0 eV band gap from our calculations) [57], the structural evolution explains the thickness-dependent MIT.

The formation of $LaNiO_{2.5}$ (A) rather than (B) and its stability decreasing with thickness also reflect the competition between the polarity discontinuity and strain effects in this system. Because the formal charge of each layer is $1+/1-$ for $LaNiO_{2.5}$ (A) but $2+/2-$ for $LaNiO_{2.5}$ (B), the polarity discontinuity effect is weaker in the former. By contrast, the lattice mismatch relative to the substrate is 4.1% for $LaNiO_{2.5}$ (A) but only -0.4% for $LaNiO_{2.5}$ (B) according to the lattice parameters of free-standing $LaNiO_{2.5}$, and therefore the strain energy is larger in the former. When the film is thin, the strain effects are weak and the less polar surface is likely to be stable, suggesting the system prefers the growth of $LaNiO_{2.5}$ (A). However, when the film becomes thick, the strain effects gradually increase, suggesting that the formation of $LaNiO_{2.5}$ (A) will become more difficult and the possible growth of $LaNiO_3$ would be expected.

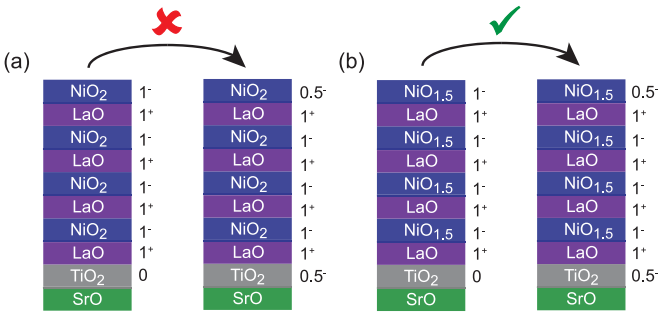

FIG. 5. Schematic illustration of how (a) $LaNiO_3$ cannot transfer electrons from the surface since Ni^{4+} is highly unstable, while for the case of (b) $LaNiO_{2.5}$, the surface valence can change to $Ni^{2.5+}$ to provide the charge needed to balance the polar discontinuity.

To understand how the V_O formation can solve the polar discontinuity, we finally examined the charge transfer between the epitaxial $LaNiO_3$ and $LaNiO_{2.5}$ (A) films and the substrates. Because the polarity mismatch induces dipoles in the growth direction, to compensate the dipole, it is necessary to transfer electrons from the top region of the epitaxial film to the bottom region, as schematically shown in Fig. 5. However, such electron transfer is energetically unfavorable for $LaNiO_3$ because the valance state of Ni is already at the maximum value of 3+. In contrast, the V_O in $LaNiO_{2.5}$ (A) reduces Ni to 2+ and thus allows it to lose electrons and compensate the polarity mismatch. This simplified model is qualitatively supported by our DFT results that show for a thickness of 2, 4, and 7 u.c., the electron transfer from $LaNiO_3$ to the substrate is only 0.17 electrons per surface Ni atom regardless of thickness, but for $LaNiO_{2.5}$ it is 0.24, 0.30, and 0.31 electrons per surface Ni atom, respectively. Figure 1(b) suggests that such charge transfer possibly does not lead to a two-dimensional electron gas but only immobile charge states, as observed in other systems [60,61]. To further support that this $LaNiO_{2.5}$ structure is stable, we considered a plausible competing structure that also compensates polarity, namely, an epitaxial $LaNiO_3$ film terminated with a top oxygen-deficient $NiO_{1.5}$ surface. The comparison shown in Fig. S2 in the Supplemental Material [55] indicates that $LaNiO_{2.5}$ is the most stable structure under synthesis conditions. The DFT results also reveal that major electron loss occurs in the top three atomic layers and the extra electrons aggregate in several layers above and/or below the interface. Such electron depletion and aggregation in the top and bottom regions of the epitaxial $LaNiO_{2.5}$ films are consistent with the positive and negative ΔB in the two regions [Fig. 2(c)], respectively. Note that in our measurement we only measure the average atomic position of the layer so we cannot distinguish a rumpling of the BO_2 plane vs off-centering. However, previous work has shown that both the rumpling and off-centering are correlated with changes in the valence of ions near the interface [48,50]. One implication of the simple picture of charge transfer developed here is that similar V_O formation is expected to occur in the growth of other polar ABO_3 on STO, if the maximum valance state of B is 3+, such as Al [62], Fe, and Co, and the oxidizing environment is not exceptionally strong [55]. By contrast, the polar material is expected to grow without or with only a few V_O, if B has a maximum valance state greater than 3+, such as V, Cr, and Mn.

IV. CONCLUSIONS

In conclusion, we have combined theory and experiment to understand how ultrathin $LaNiO_3$ forms an oxygen-deficient phase in order to resolve the polar mismatch on $SrTiO_3$. This transition from a nonstoichiometric phase to the expected one shows clearly a mechanism for the MIT that occurs when the layers are thin. This demonstrates pathways by which ABO_3 materials can fluctuate from B^{3+} to B^{2+} coupled with oxygen vacancy formation within the BO_2 layers in order to resolve the polar discontinuity.

ACKNOWLEDGMENTS

Work at the Advanced Photon Source, Argonne was supported by the U.S. Department of Energy, Office of Science under Grant No. DEAC02-06CH11357. *In situ* x-ray measurements were supported by the U.S. Department of Energy, Office of Science, Basic Energy Sciences, Materials Sciences and Engineering Division. G.L. and D.M. were partially supported by University of Wisconsin Materials Research Science and Engineering Center (DMR-1121288). Computing resources in this work benefited from the use of the Extreme Science and Engineering Discovery Environment (XSEDE), which is supported by National Science Foundation Grant No. ACI-1053575, and the compute resources and assistance of the UW-Madison Center For High Throughput Computing (CHTC) in the Department of Computer Sciences.

[1] Y. Tokura and N. Nagaosa, Science **288**, 462 (2000).
[2] M. Bibes, J. E. Villegas, and A. Barthelemy, Adv. Phys. **60**, 5 (2011).
[3] J. Rondinelli, S. May, and J. Freeland, MRS Bull. **37**, 261 (2012).
[4] J. Chakhalian, J. W. Freeland, A. J. Millis, C. Panagopoulos, and J. M. Rondinelli, Rev. Mod. Phys. **86**, 1189 (2014).
[5] C. Noguera, J. Phys.: Condens. Matter **12**, R367 (2000).
[6] J. Goniakowski, F. Finocchi, and C. Noguera, Rep. Prog. Phys. **71**, 016501 (2008).
[7] A. Kahn, Surf. Rev. Lett. **3**, 1579 (1999).
[8] N. Nakagawa, H. Hwang, and D. Muller, Nat. Mater. **5**, 204 (2006).
[9] J. Mannhart, D. H. A. Blank, H. Y. Hwang, A. J. Millis, and J. M. Triscone, MRS Bull. **33**, 1027 (2008).
[10] P. Zubko, S. Gariglio, M. Gabay, P. Ghosez, and J.-M. Triscone, Annu. Rev. Condens. Matter Phys. **2**, 141 (2011).
[11] H. Y. Hwang, Y. Iwasa, M. Kawasaki, B. Keimer, N. Nagaosa, and Y. Tokura, Nat. Mater. **11**, 103 (2012).
[12] S. Hong, S. M. Nakhmanson, and D. D. Fong, Rep. Prog. Phys. **79**, 076501 (2016).
[13] S. V. Kalinin, A. Borisevich, and D. Fong, ACS Nano **6**, 10423 (2012).
[14] Y.-L. Lee and D. Morgan, Phys. Rev. B **91**, 195430 (2015).

[15] J. Chaloupka and G. Khaliullin, Phys. Rev. Lett. **100**, 016404 (2008).

[16] P. Hansmann, X. Yang, A. Toschi, G. Khaliullin, O. K. Andersen, and K. Held, Phys. Rev. Lett. **103**, 016401 (2009).

[17] M. J. Han, X. Wang, C. A. Marianetti, and A. J. Millis, Phys. Rev. Lett. **107**, 206804 (2011).

[18] A. X. Gray, A. Janotti, J. Son, J. M. LeBeau, S. Ueda, Y. Yamashita, K. Kobayashi, A. M. Kaiser, R. Sutarto, H. Wadati *et al.*, Phys. Rev. B **84**, 075104 (2011).

[19] D. P. Kumah, A. S. Disa, J. H. Ngai, H. Chen, A. Malashevich, J. W. Reiner, S. Ismail-Beigi, F. J. Walker, and C. H. Ahn, Adv. Mater. **26**, 1935 (2014).

[20] P. D. C. King, H. I. Wei, Y. F. Nie, M. Uchida, C. Adamo, S. Zhu, X. He, I. Božović, D. G. Schlom, and K. M. Shen, Nat. Nanotechnol. **9**, 443 (2014).

[21] J. Son, J. M. Lebeau, S. J. Allen, and S. Stemmer, Appl. Phys. Lett. **97**, 202109 (2010).

[22] J. Liu, S. Okamoto, M. van Veenendaal, M. Kareev, B. Gray, P. Ryan, J. W. Freeland, and J. Chakhalian, Phys. Rev. B **83**, 161102 (2011).

[23] H. K. Yoo, S. I. Hyun, Y. J. Chang, L. Moreschini, C. H. Sohn, H.-D. Kim, A. Bostwick, E. Rotenberg, J. H. Shim, and T. W. Noh, Phys. Rev. B **93**, 035141 (2016).

[24] R. Scherwitzl, S. Gariglio, M. Gabay, P. Zubko, M. Gibert, and J.-M. Triscone, Phys. Rev. Lett. **106**, 246403 (2011).

[25] A. Kaiser, A. Gray, G. Conti, J. Son, A. Greer, A. Perona, A. Rattanachata, A. Saw, A. Bostwick, S. Yang *et al.*, Phys. Rev. Lett. **107**, 116402 (2011).

[26] H. K. Yoo, Y. J. Chang, L. Moreschini, H.-D. Kim, C. H. Sohn, S. Sinn, J. S. Oh, C.-T. Kuo, A. Bostwick, E. Rotenberg *et al.*, Appl. Phys. Lett. **106**, 121601 (2015).

[27] S. Johnston, A. Mukherjee, I. Elfimov, M. Berciu, and G. A. Sawatzky, Phys. Rev. Lett. **112**, 106404 (2014).

[28] J. Liu, M. Kareev, S. Prosandeev, B. Gray, P. Ryan, J. W. Freeland, and J. Chakhalian, Appl. Phys. Lett. **96**, 133111 (2010).

[29] E. Detemple, Q. M. Ramasse, W. Sigle, G. Cristiani, H. U. Habermeier, E. Benckiser, A. V. Boris, A. Frano, P. Wochner, M. Wu *et al.*, Appl. Phys. Lett. **99**, 211903 (2011).

[30] S. Middey, P. Rivero, D. Meyers, M. Kareev, X. Liu, Y. Cao, J. W. Freeland, S. Barraza-Lopez, and J. Chakhalian, Sci. Rep. **4**, 6819 (2014).

[31] C. L. Flint, H. Jang, J. S. Lee, A. T. N'Diaye, P. Shafer, E. Arenholz, and Y. Suzuki, Phys. Rev. Mater. **1**, 024404 (2017).

[32] D. G. Schlom, APL Mater. **3**, 062403 (2015).

[33] J. H. Lee, I. C. Tung, S. H. Chang, A. Bhattacharya, D. D. Fong, J. W. Freeland, and H. Hong, Rev. Sci. Instrum. **87**, 013901 (2016).

[34] G. Koster, B. L. Kropman, G. J. H. M. Rijnders, D. H. A. Blank, and H. Rogalla, Appl. Phys. Lett. **73**, 2920 (1998).

[35] J. Son, P. Moetakef, J. M. Lebeau, D. Ouellette, L. Balents, S. J. Allen, and S. Stemmer, Appl. Phys. Lett. **96**, 062114 (2010).

[36] S. J. May, J. W. Kim, J. M. Rondinelli, E. Karapetrova, N. A. Spaldin, A. Bhattacharya, and P. J. Ryan, Phys. Rev. B **82**, 014110 (2010).

[37] E. J. Moon, B. A. Gray, M. Kareev, J. Liu, S. G. Altendorf, F. Strigari, L. H. Tjeng, J. W. Freeland, and J. Chakhalian, New J. Phys. **13**, 073037 (2011).

[38] J. W. Freeland, M. van Veenendaal, and J. Chakhalian, J. Electron. Spectrosc. Relat. Phenom. **208**, 56 (2016).

[39] Y. Yacoby, M. Sowwan, E. Stern, J. O. Cross, D. Brewe, R. Pindak, J. Pitney, E. M. Dufresne, and R. Clarke, Nat. Mater. **1**, 99 (2002).

[40] R. Scherwitzl, P. Zubko, I. G. Lezama, S. Ono, A. F. Morpurgo, G. Catalan, and J.-M. Triscone, Adv. Mater. **22**, 5517 (2010).

[41] J. Chakhalian, J. Rondinelli, J. Liu, B. Gray, M. Kareev, E. Moon, N. Prasai, J. Cohn, M. Varela, I. Tung *et al.*, Phys. Rev. Lett. **107**, 116805 (2011).

[42] I. C. Tung, P. V. Balachandran, J. Liu, B. A. Gray, E. A. Karapetrova, J. H. Lee, J. Chakhalian, M. J. Bedzyk, J. M. Rondinelli, and J. W. Freeland, Phys. Rev. B **88**, 205112 (2013).

[43] B. Berini, N. Keller, Y. Dumont, E. Popova, W. Noun, M. Guyot, J. Vigneron, A. Etcheberry, N. Franco, and R. M. C. da Silva, Phys. Rev. B **76**, 205417 (2007).

[44] M. Kawai, S. Inoue, M. Mizumaki, N. Kawamura, N. Ichikawa, and Y. Shimakawa, Appl. Phys. Lett. **94**, 082102 (2009).

[45] P. R. Willmott, S. A. Pauli, R. Herger, C. M. Schleputz, D. Martoccia, B. D. Patterson, B. Delley, R. Clarke, D. Kumah, C. Cionca *et al.*, Phys. Rev. Lett. **99**, 155502 (2007).

[46] C. L. Jia, S. B. Mi, M. Faley, U. Poppe, J. Schubert, and K. Urban, Phys. Rev. B **79**, 081405 (2009).

[47] S. A. Pauli, S. J. Leake, B. Delley, M. Björck, C. W. Schneider, C. M. Schleputz, D. Martoccia, S. Paetel, J. Mannhart, and P. R. Willmott, Phys. Rev. Lett. **106**, 036101 (2011).

[48] C. Cancellieri, D. Fontaine, S. Gariglio, N. Reyren, A. D. Caviglia, A. Fête, S. J. Leake, S. A. Pauli, P. R. Willmott, M. Stengel *et al.*, Phys. Rev. Lett. **107**, 056102 (2011).

[49] T. T. Fister, H. Zhou, Z. Luo, S. S. A. Seo, S. O. Hruszkewycz, D. L. Proffit, J. A. Eastman, P. H. Fuoss, P. M. Baldo, H. N. Lee *et al.*, APL Mater. **2**, 021102 (2014).

[50] P. W. Lee, V. N. Singh, G. Y. Guo, H. J. Liu, J. C. Lin, Y.-H. Chu, C. H. Chen, and M. W. Chu, Nat. Commun. **7**, 12773 (2016).

[51] G. Kresse and J. Furthmüller, Comput. Mater. Sci. **6**, 15 (1996).

[52] G. Kresse and J. Furthmüller, Phys. Rev. B **54**, 11169 (1996).

[53] Y.-L. Lee, J. Kleis, J. Rossmeisl, and D. Morgan, Phys. Rev. B **80**, 224101 (2009).

[54] L. Wang, T. Maxisch, and G. Ceder, Phys. Rev. B **73**, 195107 (2006).

[55] See Supplemental Material at http://link.aps.org/supplemental/10.1103/PhysRevMaterials.1.053404 for additional data and details on sample growth, characterization, and DFT calculations.

[56] M. Crespin, P. Levitz, and L. Gatineau, J. Chem. Soc., Faraday Trans. 2 **79**, 1181 (1983).

[57] R. D. Sánchez, M. T. Causa, A. Caneiro, A. Butera, M. Vallet-Regí, M. J. Sayagués, J. González-Calbet, F. García-Sanz, and J. Rivas, Phys. Rev. B **54**, 16574 (1996).

[58] J. Gázquez, S. Bose, M. Sharma, M. A. Torija, S. J. Pennycook, C. Leighton, and M. Varela, APL Mater. **1**, 012105 (2013).

[59] H. Jeen, Z. Bi, W. S. Choi, M. F. Chisholm, C. A. Bridges, M. P. Paranthaman, and H. N. Lee, Adv. Mater. **25**, 6459 (2013).

[60] M. P. Warusawithana, C. Richter, J. A. Mundy, P. Roy, J. Ludwig, S. Paetel, T. Heeg, A. A. Pawlicki, L. F. Kourkoutis, M. Zheng *et al.*, Nat. Commun. **4**, 2351 (2013).

[61] A. Rubano, G. De Luca, J. Schubert, Z. Wang, S. Zhu, D. G. Schlom, L. Marrucci, and D. Paparo, Appl. Phys. Lett. **107**, 101603 (2015).

[62] L. Yu and A. Zunger, Nat. Commun. **5**, 5118 (2014).